

Full length article

Physical properties of the type-I clathrate phase $\text{Ba}_{8-x}\text{Eu}_x\text{Au}_y\text{Si}_{46-y}$

P. Tomeš*, T. Himmelbauer, A. Sidorenko, X. Yan, A. Prokofiev, S. Paschen

*Institute of Solid State Physics, TU Wien, Wiedner Hauptstr. 8-10, 1040, Vienna, Austria*

ARTICLE INFO

Article history:

Received 23 January 2017

Received in revised form

20 February 2017

Accepted 22 February 2017

Available online 27 February 2017

2010 MSC:

72.15.Jf

Keywords:

Intermetallic compounds

Single crystal

Transport properties

Rare earth

Ferromagnetic

ABSTRACT

The effect of the substitution of rare-earth atoms for guest atoms on the low-temperature transport and magnetic properties is investigated for single-crystalline type-I clathrates with the nominal composition $\text{Ba}_{8-x}\text{Eu}_x\text{Au}_y\text{Si}_{46-y}$ ($x = 1.0, 1.68$ and $y = 4.77, 5.32$). The Seebeck coefficient and Hall coefficient data show that a transition from *n*- to *p*-type conduction takes place with increasing Au content. The *n*-type sample presents a large maximum in the thermal conductivity due to the freezing of three phonon Umklapp scattering processes at low temperatures, whereas the maximum of thermal conductivity in the *p*-type sample is strongly reduced due to dominant phonon-electron scattering process. Both samples are metal-like and ferromagnetic, with Curie temperatures T_C of 3.1 K and 10.0 K for $x = 1.0$ and 1.68, respectively. The magnetization measurement confirmed the Eu^{2+} state in both samples and the Ruderman-Kittel-Kasuya-Yoshida (RKKY) interaction model explains the FM-type of order in which the nearest-neighbor (NNN) and the next-nearest-neighbor (NN) interactions play a major role at $x = 1.0$ and 1.68, respectively.

© 2017 Acta Materialia Inc. Published by Elsevier Ltd. All rights reserved.

1. Introduction

Intermetallic cage compounds such as the type-I clathrates have been considered as promising compounds for the development of thermoelectric (TE) materials. Type-I clathrates have a cubic unit cell and an open crystal structure. The sp^3 hybridized framework contains two types of cages, the smaller pentagonal dodecahedron and the larger tetrakaidecahedron (2 and 6 per unit cell, respectively) where guest atoms are situated [1]. Type-I clathrates have generally been considered to fulfill the criteria of the phonon glass-electron crystal (PGEC) concept in which the thermal conductivity exhibits low values similar to glasses and electronic properties are similar to good semiconductor/metal single crystals. However, recent work on clathrates has cast doubts on the general validity of the PGEC concept. For example, it was shown for the type-I clathrate $\text{Ba}_8\text{Ni}_{3.5}\text{Ge}_{42.1}\square_{0.4}$ [2] that the Ba atoms cannot be considered as independent "rattlers", isolated from the host cage, because the vibrational modes of the guest atoms hybridize with the framework-derived acoustic phonon modes over a wide region of the Brillouin zone. Based on these results, an alternative mechanism of low-pass filtering of acoustic phonon modes was introduced to explain the low lattice thermal conductivity in clathrates

[3,4]. Low thermal conductivity materials are of interest for TE applications, and therefore the knowledge of the dominating scattering mechanism in these materials is essential.

The relatively small electrical resistivity ρ , large Seebeck coefficient S , and low thermal conductivity κ of type-I clathrates lead to relatively large dimensionless figure of merits $ZT = S^2T/\rho\kappa$ [5] in these materials, reaching for instance an experimental value of 1.35 at 900 K and with an extrapolated maximum of 1.63 at 1100 K for an *n*-type $\text{Ba}_8\text{Ga}_{16}\text{Ge}_{30}$ single crystal grown by the Czochralski technique [6]. Even the polycrystalline $\text{Ba}_8\text{Ga}_{16}\text{Ge}_{30}$ samples demonstrated comparable TE performance to single crystal at high temperatures via the optimization of the charge carrier concentration [7]. Also Si-based systems reveal relatively high ZT values, as it was shown for $\text{Ba}_8\text{Ga}_x\text{Si}_{46-x}$, where $ZT = 0.87$ was reached at 1000 K [8]. Therefore, Si-based type-I clathrates are of interest for TE applications as well. Many attempts of substituting different transition metal elements for Si have been done in order to optimize the TE properties and enhance ZT [9–11]. Au is interesting for its large atomic radius and mass, and its high electronegativity. Detailed investigations on $\text{Ba}_8\text{Au}_x\text{Si}_{46-x}$ revealed an *n*-type/*p*-type crossover near $x = 5.33$ as the Zintl concept predicts [12]. TE property measurements reveal relatively high S and low κ values, but the electrical resistivity still remains a limiting factor for achieving ZT higher than ≈ 0.2 [11]. Si-based type-I clathrates have also attracted attention due to the occurrence of

* Corresponding author.

E-mail address: petr.tomes@ifp.tuwien.ac.at (P. Tomeš).

superconductivity below 8 K in $\text{Ba}_8\text{Si}_{46}$ [13,14]. Among the rare-earth containing type-I clathrate systems, only for Eu a full occupation of all guest sites has been observed [15,16]. This is due to a large ionic radius of the divalent and earth alkali-like Eu in the $4f^7$ ground state, which has stabilizing effect for substitution for Ba and Sr, for instance in $\text{Eu}_2\text{Ba}_6\text{Ga}_8\text{Si}_{36}$ and $\text{Eu}_1\text{Sr}_7\text{Al}_{10}\text{Si}_{36}$. Eu tends to occupy the smaller cage in the clathrate framework [17].

The preferential Eu occupancy of the smaller cages was confirmed by resonant X-ray scattering [18]. Eu-containing type-I clathrates are also of interest because Eu^{2+} carries a large magnetic moment, and because the Seebeck coefficient is relatively high and the thermal conductivity is low.

An investigation of a series of the rare earth substituted $\text{Ba}_{8-x}\text{RE}_x\text{Au}_y\text{Si}_{46-y}$ clathrates revealed a rather high substitution level for Eu reaching about 1.5 per formula unit (f.u.) [19]. In this work we report on the low-temperature transport and magnetic properties of single-crystalline $\text{Ba}_{8-x}\text{Eu}_x\text{Au}_y\text{Si}_{46-y}$ ($x = 1.0, 1.68$ and $y = 4.77, 5.32$) type-I clathrates. We focus on the substitution effects of Au for Si as electron acceptor and of Eu for Ba as heavier element with magnetic moment on the electrical and thermal transport. Additionally, detailed investigations of magnetic properties are discussed.

2. Experimental

2.1. Synthesis

Polycrystalline samples for crystal growth were synthesized by melting Ba (99.5%), Eu (99.9%), Au (99.95%), and Si (99.9999%) in a horizontal water cooled copper boat in argon atmosphere (6N) using high-frequency heating. The samples were homogenized by three remeltings. Single crystals of $\text{Ba}_{8-x}\text{Eu}_x\text{Au}_y\text{Si}_{46-y}$ were grown using a floating zone technique with optical heating in a four mirror furnace (Crystal Corporation).

2.2. X-ray analysis

The crystal structure and phase purity of the samples were studied by X-ray powder diffraction (XPD) using a PANalytical X'Pert II diffractometer with $\text{Cu}-\text{K}\alpha_{1,2}$ radiation at room temperature. The crystallographic parameters were obtained from Rietveld refinements using the Fullprof Suite software [20].

2.3. SEM/EDX

The phase compositions on polished samples were determined using scanning electron microscopy with energy dispersive X-ray spectroscopy (SEM/EDX) in a Philips XL30 ESEM with an excitation of 30 keV. The standard deviation δ of the composition with a maximum of $\delta_{max} = 0.11$ at. % refers to spatial inhomogeneity of the sample and it does not contain systematic error of used method. The error was estimated from a series of measurements at different positions of the sample.

2.4. Physical properties

The electrical resistivity ρ and the Hall effect were measured using a Physical Property Measurement System (PPMS, Quantum Design, $B = 9$ T) in the temperature range $2 \text{ K} < T < 300 \text{ K}$ with a 6-point quasi AC technique in the PPMS using a horizontal rotator. For Hall effect measurements thin platelets samples were prepared in order to enhance the Hall voltage. The Hall resistivity ρ_H was measured in magnetic fields up to 9 T. In order to eliminate the misalignment voltage, ρ_H was measured at the angles 0° and 180°

between the sample normal and the magnetic field. Heat capacity was measured on samples of ≈ 15 mg using a relaxation-type technique in a PPMS in the temperature range $1.8 \text{ K} < T < 300 \text{ K}$. The samples were attached to the sample holder using thermal conduction paste Apiezon N, which was afterwards subtracted from the total signal.

The molar magnetic susceptibility χ ($\chi = M/H$) was measured using a superconducting quantum interference device (SQUID) magnetometer in the temperature range $2 \text{ K} < T < 300 \text{ K}$ and in a field of $B = 0.1$ T. A field of $B = 2$ mT was applied during field cooling (FC) and zero field cooling (ZFC) experiments. The magnetization M was measured in varying magnetic fields (0–7 T).

The Seebeck coefficient and thermal conductivity measurements were carried in a home-made device designed for a ${}^4\text{He}$ flow cryostat, using a steady state heat flow method in the temperature range $4 \text{ K} < T < 300 \text{ K}$. The temperature gradient along the sample is applied by a small resistance-chip heater with a room-temperature resistance of $10 \text{ k}\Omega$. The heater is thermally decoupled from the sample holder through four manganin wires with a diameter of $25 \mu\text{m}$ and length of $\approx 10 \text{ cm}$. The temperature gradient along the sample was determined by a differential type-E thermocouple consisting of Chromel and Constantan. The thermal voltages were measured using manganin wires with a diameter of $25 \mu\text{m}$. The absolute temperature was measured by a Cernox thermometer in the entire investigated temperature range. A radiation shield was mounted around the sample in order to reduce the radiation effect.

3. Results and discussions

3.1. Phase analysis and structural properties

The single crystal grown by the floating zone technique is shown in Fig. 1. Single crystal $\text{Ba}_{8-x}\text{Eu}_x\text{Au}_y\text{Si}_{46-y}$ was grown according to a technique developed in Ref. [21]. The nominal composition obtained from energy dispersive x-ray spectroscopy (EDX) data revealed a gradual change in the composition of $\text{Ba}_{8-x}\text{Eu}_x\text{Au}_y\text{Si}_{46-y}$ along the crystal growth direction, while no sizable change in the composition was observed in the direction perpendicular to the crystal growth. The selected samples A and B, marked in Fig. 1, were used for physical and structural property measurements. EDX measurements revealed that both samples are homogeneous, impurity-free, and have the composition $\text{Ba}_{6.63 \pm 0.04}\text{Eu}_{1.0 \pm 0.04}\text{Au}_{4.77 \pm 0.10}\text{Si}_{41.60 \pm 0.11}$ and $\text{Ba}_{6.0 \pm 0.02}\text{Eu}_{1.68 \pm 0.04}\text{Au}_{5.32 \pm 0.06}\text{Si}_{41.0 \pm 0.04}$ for the sample A and sample B, respectively (see Table 1).

Rietveld refinements revealed that the x-ray powder diffraction (XPD) data of both samples, shown in Fig. 2, are well described by the space group $Pm-3n$ (Table 1). Because Eu and Ba are hardly distinguishable due to their close x-ray atomic scattering factors the Eu content and the Eu site occupation were not refined. The former was adopted from the EDX measurements and the latter was fixed as $2a$ based on previous investigations [17,18]. Further refinements revealed that, as common in transition metal-containing clathrates, Au atoms share the $6c$ site with Si atoms. In order to improve the reliability factors and obtain reasonable temperature factors of each crystallographic site, a small amounts of Au atoms at the $24k$ site was refined for both samples and a small amount of vacancies at the $2a$ site for the sample B. The refined compositions are $\text{Ba}_{7.0}\text{Eu}_{1.0}\text{Au}_{5.16}\text{Si}_{41.84}$ and $\text{Ba}_{6.19}\text{Eu}_{1.68}\text{Au}_{5.89}\text{Si}_{40.11}$ for the sample A and B, respectively, have a slightly larger amount of Au content than the composition determined by EDX measurements. According to XPD, the lattice parameter a of sample A and B is $1.03898(4)$ nm and $1.03835(2)$ nm, respectively. The small difference in a may be related to the different Ba/Eu and Au/Si ratios.

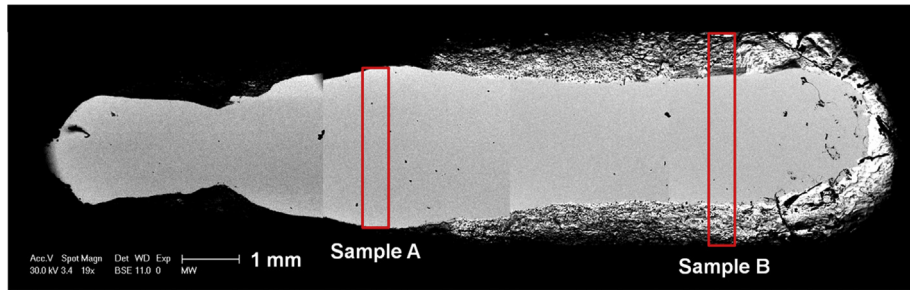


Fig. 1. SEM image of the polished surface of the single-crystalline $\text{Ba}_{8-x}\text{Eu}_x\text{Au}_y\text{Si}_{46-y}$ type-I clathrate. Two slices/samples marked with red rectangles were selected for physical and structural property measurements. (For interpretation of the references to colour in this figure legend, the reader is referred to the web version of this article.)

Table 1

Sample code, composition from EDX, and structure data from Rietveld refinement for $\text{Ba}_{8-x}\text{Eu}_x\text{Au}_y\text{Si}_{46-y}$. The data have been standardized by the program Structure Tidy [22].

Code	Sample A	Sample B
Composition/EDX	$\text{Ba}_{6.63 \pm 0.04}\text{Eu}_{1.0 \pm 0.04}\text{Au}_{4.77 \pm 0.10}\text{Si}_{41.60 \pm 0.11}$	$\text{Ba}_{6.0 \pm 0.02}\text{Eu}_{1.68 \pm 0.04}\text{Au}_{5.32 \pm 0.06}\text{Si}_{41.0 \pm 0.04}$
Composition/refined	$\text{Ba}_{7.0}\text{Eu}_{1.0}\text{Au}_{5.16}\text{Si}_{41.84}$	$\text{Ba}_{6.19}\text{Eu}_{1.68}\text{Au}_{5.89}\text{Si}_{40.11}$
a (nm)	1.03898(4)	1.03835(2)
$R_F = \sum F_0 - F_c / \sum F_0$	0.074	0.042
$R_I = \sum I_0 - I_c / \sum I_0$	0.080	0.059
$R_{WP} = [\sum w_i y_{oi} - y_{ci} ^2 / \sum w_i y_{oi} ^2]^{1/2}$	0.080	0.079
$R_P = \sum y_{oi} - y_{ci} / \sum y_{oi} $	0.052	0.055
$R_e = [(N - P + C) / (\sum w_i y_{oi}^2)]^{1/2}$	0.024	0.022
$\chi^2 = (R_{WP}/R_e)^2$	11.10	12.80
M1, in $2a$ (0, 0, 0), Occ.	1.0(1) $\text{Ba} + 1.0\text{Eu}$	0.19(1) $\text{Ba} + 1.68\text{Eu} + 0.13\text{□}$
B_{eq} (B_{iso}) $10^2(\text{nm}^2)$	0.70(9)	0.72(9)
Ba, in $6d$ ($\frac{1}{4}, 0, \frac{1}{2}$) B_{eq} (B_{iso}) $10^2(\text{nm}^2)$	1.51(9)	1.82(9)
M2, in $6c$ ($\frac{1}{4}, \frac{1}{2}, 0$), Occ.	5.04(3) $\text{Au} + 0.96\text{Si}$	5.47(3) $\text{Au} + 0.53\text{Si}$
B_{eq} (B_{iso}) $10^2(\text{nm}^2)$	0.36(9)	0.71(8)
Si in $16i$ (x, x, x), x	0.1844(6)	0.1786(4)
B_{eq} (B_{iso}) $10^2(\text{nm}^2)$	0.98(9)	0.32(9)
M3, in $24k$ (0, y, z), y, z	0.1219(6), 0.3030(6)	0.1247(7), 0.3031(5)
M3, Occ.	23.88(2) $\text{Si} + 0.12\text{Au}$	23.58(2) $\text{Si} + 0.42\text{Au}$
B_{eq} (B_{iso}) $10^2(\text{nm}^2)$	0.30(9)	0.65(7)

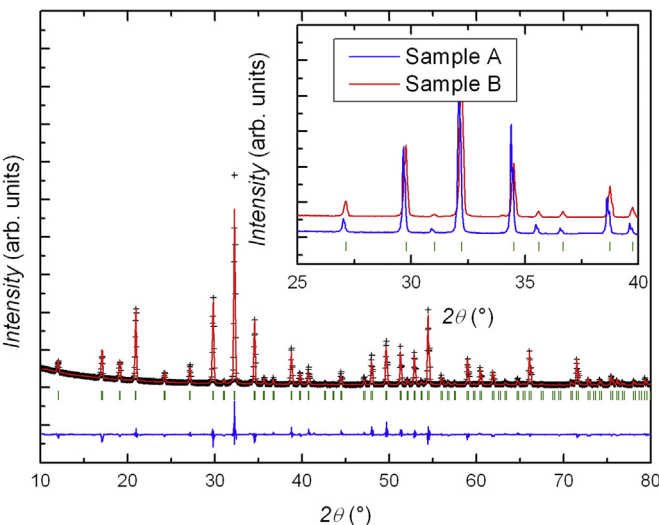


Fig. 2. Rietveld refinement of the XPD data of the sample B. The observed (black across) and calculated (red line) intensities, difference curve (blue line), and Bragg positions (green line) are shown. The inset shows the XPD of both samples to clarify the phase purity and peak shifts due to different lattice parameters. (For interpretation of the references to colour in this figure legend, the reader is referred to the web version of this article.)

The larger content of the smaller Eu in sample B should lead to a lattice shrinking which is, however, compensated by a higher

content of larger Au [23]. The Eu substitution for Ba affects lattice parameter more efficiently compared to the Au substitution for Si due to the saturation effect for a high Au content ($y > 5.2$) observed in Ref. [12], therefore, a (sample A) $>$ a (sample B).

3.2. Electronic properties

Overall, the electrical resistivities of $\text{Ba}_{8-x}\text{Eu}_x\text{Au}_y\text{Si}_{46-y}$ show metal-like characteristic ($\Delta\rho/\Delta T > 0$), with the room-temperature values of 1.62 and 1.23 mΩ cm for sample A and B, respectively (Fig. 3a). At low-temperatures, anomalies in $\rho(T)$, with their origin presumably in the ferromagnetic phase transition, are observed. The transition has been confirmed by heat capacity and magnetic susceptibility measurements (see later) – which revealed the Curie temperatures $T_C \approx 3$ K and 10 K for sample A and B, respectively (see Table 2).

Whereas the sample B clearly exhibits the electrical resistivity maximum at T_C of 10 K (Fig. 3c), the sample A shows an upturn in $\rho(T)$ with decreasing temperature with no distinct maximum (Fig. 3b). This is most probably due to higher degree of structural disorder at the 6c site of the framework (smaller Au content) in sample A and due to presence of additional scattering mechanism. This could explain as well lower residual resistance ratio RRR of sample A compared to sample B (see Table 2). An enhanced negative magnetoresistance (MR) near the Curie temperatures (Fig. 3d) is a result of magnetic spin disorder scattering of s electrons by the localized Eu^{2+} $4f$ electrons [16].

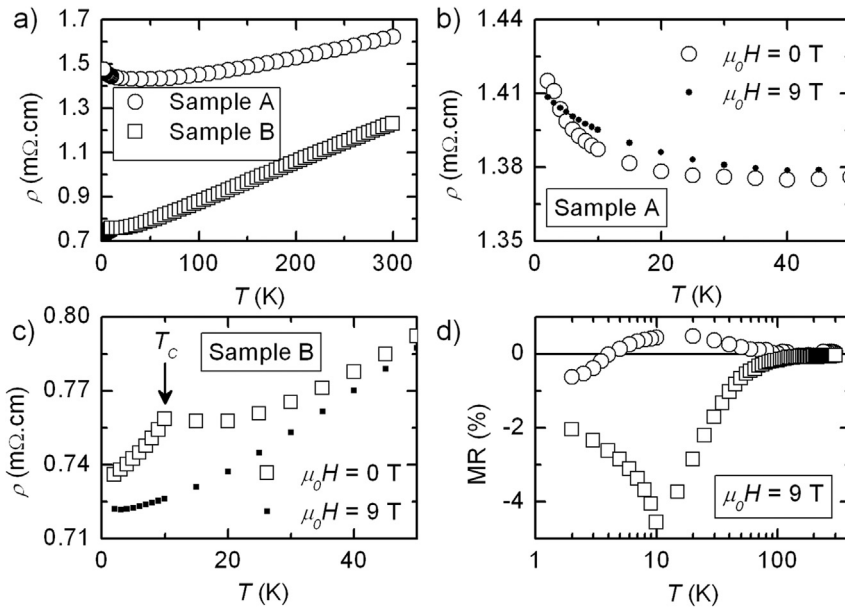


Fig. 3. (a) Temperature dependence of the electrical resistivities $\rho(T)$ of $\text{Ba}_{8-x}\text{Eu}_x\text{Au}_y\text{Si}_{46-y}$. The low-temperature closeup of ρ showing the T_c of sample A (b) and sample B (c). Temperature dependencies of the longitudinal magnetoresistance (MR) measured in applied magnetic field of 9 T.

Table 2

Residual resistance ratio $\text{RRR} = \rho(300 \text{ K})/\rho(2 \text{ K})$, Curie temperatures T_{C,C_p} and $T_{C,\chi}$ determined from heat capacity and from the magnetic susceptibility, respectively, Weiss temperature Θ , Hall coefficient R_H , normal Hall coefficient R_0 and spontaneous Hall coefficient R_S at 2 K, charge carrier concentration n at 300 K and 2 K.

Code	RRR	T_{C,C_p} (K)	$T_{C,\chi}$ (K)	Θ (K)	$ R_H $ (2 K) ($10^{-9}/\text{m}^3 \text{ C}^{-1}$)	$ R_0 $ (2 K) ($10^{-9}/\text{m}^3 \text{ C}^{-1}$)	$ R_S $ (2 K) ($10^{-9}/\text{m}^3 \text{ C}^{-1}$)	$ n $ (300 K) ($10^{27}/\text{m}^3$)	$ n $ (2 K) ($10^{27}/\text{m}^3$)
Sample A	1.1	3.1	4.1	6.0	2.83	3.40	5.39	2.38	2.21
Sample B	1.7	10.0	11.1	10.6	15.41	3.33	79.12	1.60	0.40

Fig. 4 shows the magnetic field-dependent Hall resistivities $\rho_H(\mu_0 H)$ at several temperatures. ρ_H is linear in $\mu_0 H$ at temperatures above T_C , but deviates from linearity below T_C . Taking into account these observations, a one-band approach can be applied for the Hall

coefficient R_H evaluation above T_C . **Fig. 5a** shows that R_H is negative for sample A, and positive for sample B, pointing to the dominance of electron-like and hole-like conduction, respectively. The R_H values correspond to carrier concentrations of $2.38 \cdot 10^{27} \text{ m}^{-3}$ and

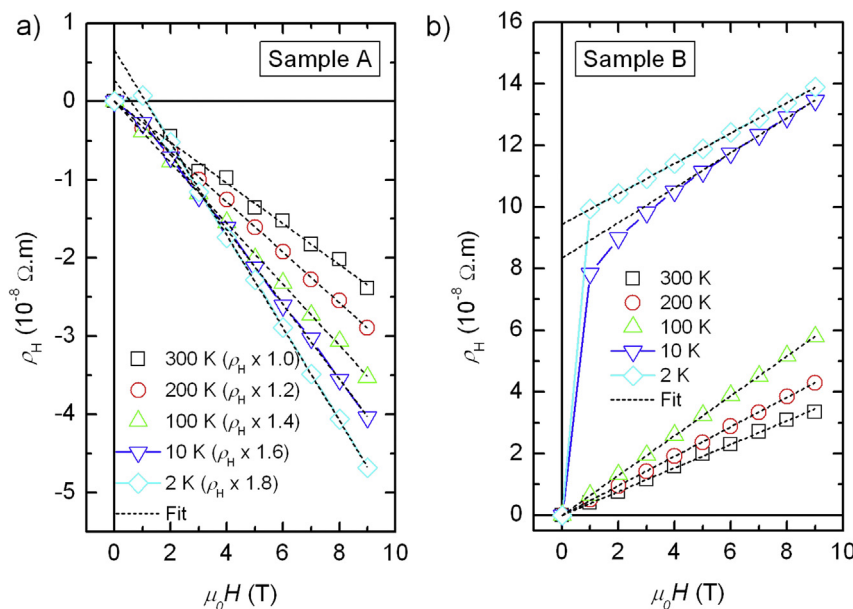


Fig. 4. ρ_H plotted as a function of the applied magnetic field $\mu_0 H$ at $T = 300 \text{ K}$ (□), 200 K (○), 100 K (△), 10 K (▽), and 2 K (◇) for (a) sample A and (b) sample B of $\text{Ba}_{8-x}\text{Eu}_x\text{Au}_y\text{Si}_{46-y}$.

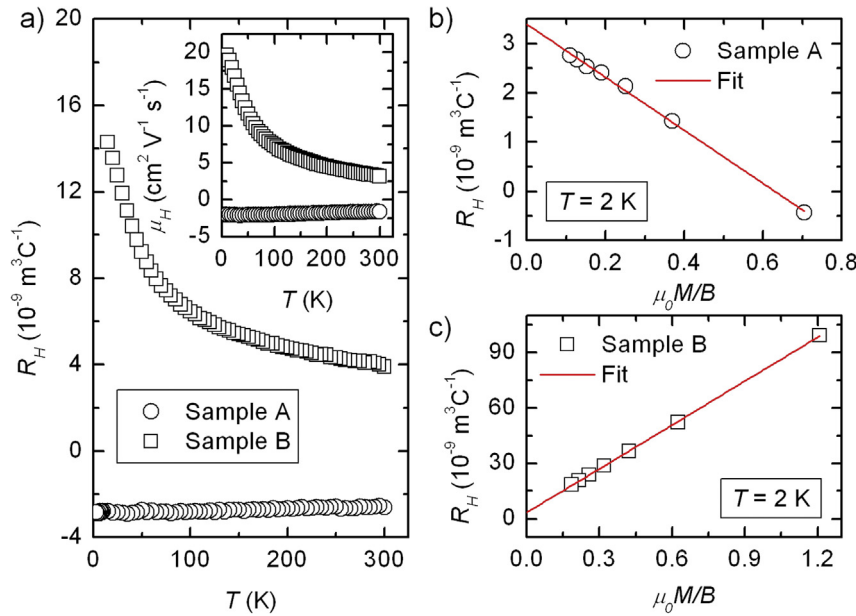


Fig. 5. (a) Temperature dependence of the Hall coefficients $R_H(T)$ above T_C of $\text{Ba}_{8-x}\text{Eu}_x\text{Au}_y\text{Si}_{46-y}$. The inset shows the temperature dependence of the Hall mobilities μ_H . $R_H(B)$ plotted vs. $\mu_0M(B)/B$ at 2 K of sample A (b) and sample B (c).

$1.60 \cdot 10^{27} \text{ m}^{-3}$ (2.67 and 1.80 per formula unit) at 300 K for the sample A and sample B, respectively (Table 3). Below T_C , the nonlinear term in $\rho_H(\mu_0H)$ is the anomalous Hall coefficient. Here, the Hall resistivity can be written as $\rho_H(B) = R_0(B) + R_s\mu_0M(B)$, where R_0 and R_s are the normal and the spontaneous Hall coefficients, respectively, μ_0 is the permeability of the vacuum, and M is the sample's volume magnetization [24]. The linear behavior of $R_H(B) = \rho_H(B)/B$ vs. $\mu_0M(B)/B$ (Fig. 5b and c) reveals the ratio R_s/R_0 of 1.6 and 23.7 for sample A and B, respectively. These values are typical for ferromagnetic semiconductors and metals, respectively [25]. The Hall mobilities μ_H , evaluated from the R_H above T_C and the electrical resistivity data as $\mu_H = R_H/\rho$, are shown in the inset of Fig. 5a. μ_H , in absolute values, reaches 1.6 and $3.2 \text{ cm}^2 \text{ V}^{-1} \text{ s}^{-1}$ at 300 K for sample A and B, respectively.

The temperature dependent Seebeck coefficients $S(T)$ are plotted in Fig. 6. The negative and positive sign of S for $\text{Ba}_{6.63}\text{Eu}_{1.0}\text{Au}_{4.77}\text{Si}_{41.6}$ and $\text{Ba}_{6.0}\text{Eu}_{1.68}\text{Au}_{5.32}\text{Si}_{41.0}$, respectively are in agreement with the Hall effect measurements. They both are also consistent with the counting based on the Zintl concept which is discussed as follows. If all hosts atoms forming a type-I clathrate framework are covalently bound to their four neighboring atoms, the charge carrier concentration can be estimated from a simple Zintl counting scheme $[\text{Ba}^{+2}]_{8-x}[\text{Eu}^{+2}]_x[\text{Au}^{-3}]_y[\text{Si}^0]_{46-y}$. From this scheme, the difference in the charge carrier concentration n , and therefore in $S(T)$ cannot be due to different substitution levels x of Eu but must be due to different Au concentrations y . This Zintl counting results in 0.95 electrons and 0.60 holes per formula unit for sample A and B, respectively, compared to 2.47 electrons and 0.45 holes per formula unit evaluated from the Hall coefficient

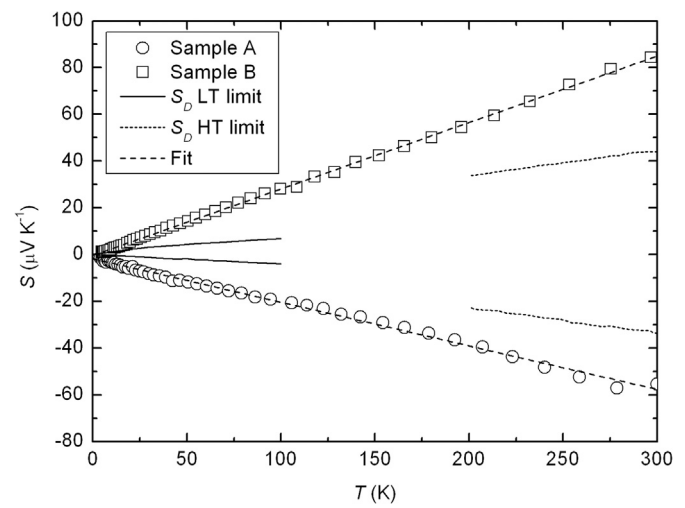


Fig. 6. Temperature dependence of the Seebeck coefficients $S(T)$ of $\text{Ba}_{8-x}\text{Eu}_x\text{Au}_y\text{Si}_{46-y}$. Solid and dotted lines represent the low- and high-temperature limits of the free-electron diffusion Seebeck coefficient S_D , and dashed lines are the linear fits of experimental data.

measurements at 2 K. The Seebeck coefficient $S(T)$ is nearly linear in T . This behavior is expected for a diffusion Seebeck coefficient S_D in the free-electron approximation [26] both at low temperatures, $S_D = \pi^2 k_B^2 2m/[3e\hbar^2(3n\pi^2)^{2/3}]T$, and at high temperatures, $S_D = \pi^2 k_B^2 2m/[\hbar^2(3n\pi^2)^{2/3}]T$, where m is the effective mass of the

Table 3

Composition from EDX, lattice parameter a from Rietveld refinement, type of major carriers, charge carrier concentration n_{exp} evaluated experimentally at 2 K and 300 K and from the Zintl concept n_{Zintl} , and the effective mass m at 300 K.

Code	Composition	a nm	p/n	$ n _{\text{exp}}$ (300 K)	$ n _{\text{exp}}$ (2 K)	$ n _{\text{Zintl}}$	m (300 K) (m_0)
Sample A	$\text{Ba}_{6.63}\text{Eu}_{1.0}\text{Au}_{4.77}\text{Si}_{41.6}$	1.03898(4)	n	2.67	2.47	0.95	3.31
Sample B	$\text{Ba}_{6.0}\text{Eu}_{1.68}\text{Au}_{5.32}\text{Si}_{41.0}$	1.03835(2)	p	1.80	0.45	0.60	3.87

charge carriers and n is the charge carrier concentrations evaluated from the R_H . The experimental data of $S(T)$ are of the same order as the diffusion Seebeck coefficient calculated from our R_H data and $m = m_0$ (see Fig. 6). We do not observe any anomaly in the linear behavior of $S(T)$ near T_C , which means that there are no sizable magnetic contributions to the Seebeck coefficient. Using the high-temperature free-electron approximation and room temperature values of n, m can be evaluated from the linear fit of $S(T)$. This yields the effective mass m of $3.31 m_0$ and $3.87 m_0$ at 300 K for sample A and B, respectively. This result is consistent with previous observations of p -type carriers in type-I clathrates being heavier than n -type carriers [27].

3.3. Thermal properties

The temperature dependence of the heat capacities $C_p(T)$ of $\text{Ba}_{8-x}\text{Eu}_x\text{Au}_y\text{Si}_{46-y}$ is shown in Fig. 7. Up to 300 K C_p remains sizably below the Dulong-Petit's limit $C_p = 3RN$, where R is the universal gas constant and N is the number of atoms per formula unit. Similar behavior was observed in several Si-based type-I clathrates [11,12]. At low temperatures, both samples show pronounced anomalies in $C_p(T)$ (see inset of Fig. 7). These anomalies are associated with ferromagnetic phase transitions, as discussed above. The Curie temperature evaluated from $C_p(T)$ is 3.1 K and 10.0 K for sample A and B, respectively.

It is known that clathrates with n -type conductivity, low charge carrier concentrations, and centered guest atoms show a large maximum in κ_{ph} due to the freezing of three phonon Umklapp scattering processes at low-temperatures [3,28]. A large maximum in κ_{ph} is indeed observed for sample A (see Fig. 8). By introducing the transition metals, which act as efficient point scattering centers, κ_{ph} can be significantly reduced. Moreover, an increase of the guest free space in type-I clathrates also reduces κ_{ph} [29–31]. These behavior were found in $\text{Ba}_8\text{Ga}_{16}\text{Ge}_{30}$, $\text{Ba}_8\text{Ni}_{6-x}\text{Ge}_{40+x}$, $\text{Ba}_8\text{Ga}_{16}\text{Sn}_{30}$, $\text{Ba}_8\text{Au}_x\text{Si}_{46-x}$, and $\text{Ba}_8\text{Au}_x\text{Ga}_{16-3x}\text{Ge}_{30+2x}$ [12,31–34]. In order to determine the reason for crystalline-like behavior of the n -type sample A compared to glass-like behavior of the p -type sample B, κ_{ph} must be first of all extracted from the total κ by subtracting of the electronic contribution κ_{el} using the Wiedemann-Franz relation, $\kappa_{el} = L_0 T/\rho$ with $L_0 = 2.44 \times 10^{-8} V^2 \text{ K}^{-2}$. κ_{el} is 13% and 21% of κ_{ph} at 150 K for sample A and B, respectively (inset of Fig. 8). Different κ_{ph} for sample A and sample B is due to different

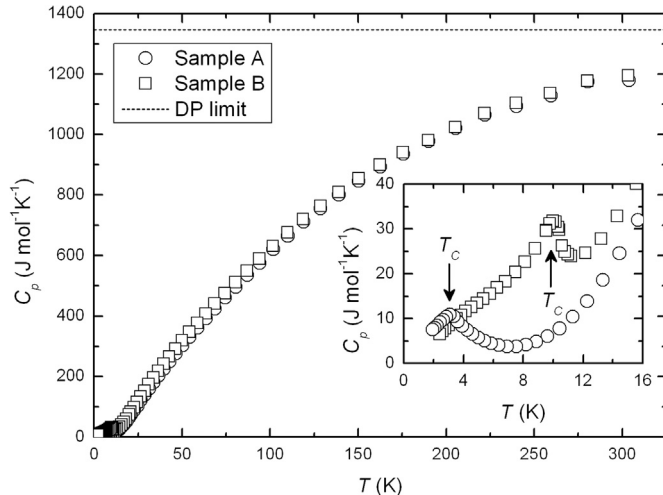


Fig. 7. Temperature dependence of the heat capacities $C_p(T)$ of $\text{Ba}_{8-x}\text{Eu}_x\text{Au}_y\text{Si}_{46-y}$ with Dulong-Petit's limit. The inset shows the low-temperature closeup of C_p showing the $T_C = 3.1$ K and 10.0 K for sample A and sample B, respectively.

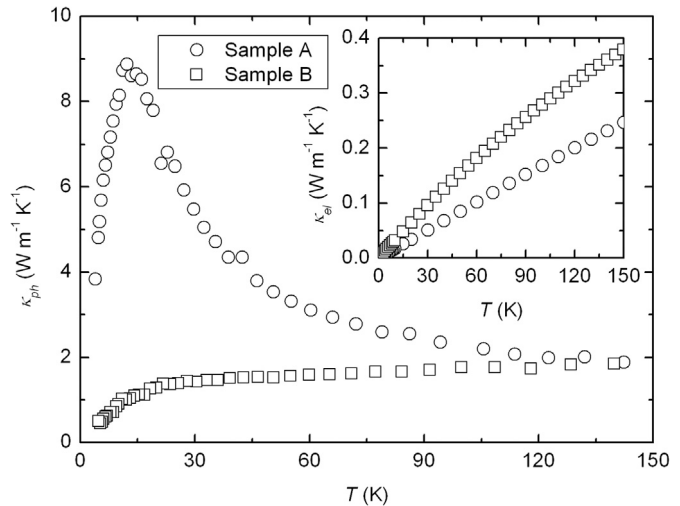


Fig. 8. Temperature dependence of the phonon thermal conductivities $\kappa_{ph}(T)$ of $\text{Ba}_{8-x}\text{Eu}_x\text{Au}_y\text{Si}_{46-y}$. The inset shows the electronic part of the thermal conductivity κ_{el} , obtained from the electrical resistivity data by using the Wiedemann-Franz relation.

scattering mechanism of phonons and/or different effective mass of holes and electrons.

3.4. Magnetic properties

The temperature dependences of the inverse magnetic susceptibility $\chi^{-1} = H/M$ of both samples measured in a magnetic field of 0.1 T, are presented in Fig. 9. The low-temperature χ measured in a magnetic field of 2 mT (inset of Fig. 9) upon zero field cooling (ZFC) and field cooling (FC) show a different behavior below T_C . While ZFC curve below ≈ 3 K and 9 K for sample A and B, respectively, slightly saturates or decreases, both FC curves below these temperatures slightly rise. This behavior is typical for a ferromagnetic phase transition. The Curie temperatures T_C of 4.1 K and 11.1 K for sample A and B, respectively, were determined as anomaly in $\partial\chi/\partial T$. Above T_C , $\chi(T)$ data are well described by the Curie-Weiss law with Weiss

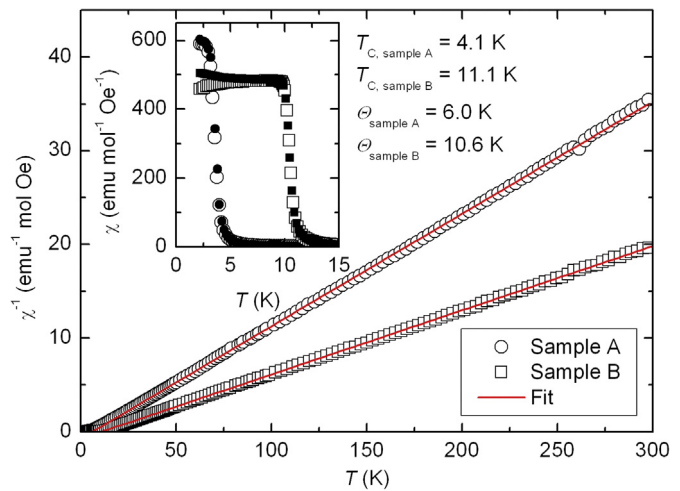


Fig. 9. Temperature dependence of the inverse magnetic susceptibilities $\chi^{-1}(T)$ of $\text{Ba}_{8-x}\text{Eu}_x\text{Au}_y\text{Si}_{46-y}$ measured in the magnetic field of 0.1 T. The Curie-Weiss fits to the χ^{-1} data above T_C in the magnetic field of 0.1 T indicate a Weiss temperatures of 6.0 K and 10.6 K for sample A and B, respectively, and an effective magnetic moment of $8.3 \mu_B$ per Eu ion for both samples. The inset shows $\chi(T)$ measured as field cooling (FC) (solid symbols) and zero field cooling (ZFC) (open symbols) with applied magnetic field of 2 mT. T_C of 4.1 K and 11.1 K was evaluated for sample A ad B, respectively.

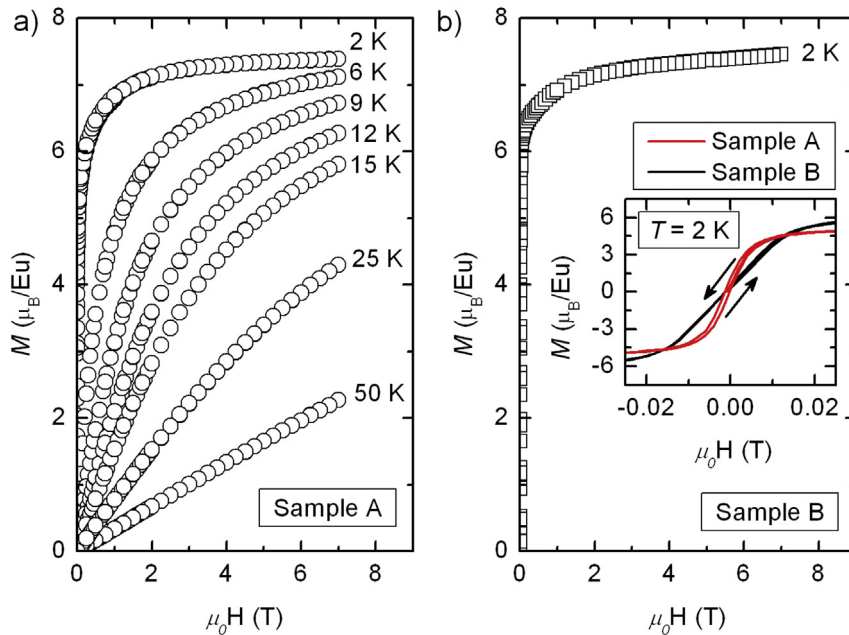


Fig. 10. Magnetization vs. magnetic field, $M(H)$, curves at different temperatures between 2 K and 50 K for sample A (a) and sample B (b). For the sake of clarity, only $M(H)$ data of 2 K for sample B are shown. The saturation magnetization is the closeup of $M(H)$ at 2 K showing a weak hysteresis loops for both samples.

temperatures Θ of 6.0 K and 10.6 K for sample A and B, respectively, and an effective magnetic moment of $8.3 \mu_B$ per Eu ion for both samples. Small and positive Weiss temperatures suggest the existence of weak ferromagnetic interactions between the magnetic moments of Eu in both samples. The effective magnetic moments are close to the effective magnetic moment of $7.93 \mu_B$ for a free Eu^{2+} ion. The small deviations might be due to crystal electric field effects or due to a slightly lower amount of Eu in the samples (see below).

Fig. 10 shows the magnetization curves as a function of magnetic field at different temperatures between 2 K and 50 K. The largest change in magnetization is observed as the temperature crosses the ferromagnetic phase transition. The magnetization is almost saturated at 2 K and at 7 T and reaches values slightly higher than the saturation magnetization of $7 \mu_B$ of a free Eu^{2+} ion. This slight discrepancy can be due to fact that the actual Eu content in both samples is larger than the nominal composition obtained from EDX. The inset of Fig. 10b is the closeup of $M(H)$ at 2 K, showing weak hysteresis loops for both samples. The origin of ferromagnetism in $\text{Ba}_{8-x}\text{Eu}_x\text{Au}_y\text{Si}_{46-y}$ is the indirect exchange interaction between 4f moments via the charge carriers [24,35], known as indirect Ruderman–Kittel–Kasuya–Yoshida (RKKY) mechanism.

4. Discussions

In order to evaluate the lattice $C_L(T)$, electronic $C_{el}(T)$, and the magnetic $C_{mag}(T)$ contributions to the total heat capacity, a nonmagnetic reference material would have to be subtracted as in Ref. [24]. Possible nonmagnetic reference materials from Ref. [12], with the compositions $\text{Ba}_8\text{Au}_{4.85}\text{Si}_{39.72}$ and $\text{Ba}_8\text{Au}_{5.59}\text{Si}_{39.01}$ close to our compositions $\text{Ba}_{6.63}\text{Eu}_{1.0}\text{Au}_{4.77}\text{Si}_{41.6}$ and $\text{Ba}_{6.0}\text{Eu}_{1.68}\text{Au}_{5.32}\text{Si}_{41.0}$, describe satisfactorily the $C_p(T)$ of our samples (see Fig. 11). The electronic heat capacity $C_{el}(T)$ of nonmagnetic samples were subtracted using the Sommerfeld coefficients from Ref. [12]. To obtain the $C_{el}(T) = \gamma T$ of sample A and B, where $\gamma = \pi^2 k_B^2 / 3 \cdot N(E_F)$ is the Sommerfeld coefficient and $N(E_F)$ is the density of states at the Fermi level E_F , $N(E_F) = mV_{f.u.}(3n)^{1/3} / \hbar^2 \pi^{4/3}$ was calculated using

the charge carrier concentrations n at 2 K, volume per formula unit $V_{f.u.}$ and effective mass m of the charge carriers equal to the free-electron mass [36]. The density of states is enhanced for sample A compared to sample B mainly due to charge carrier concentration enhancement in sample A (see Table 4).

The magnetic contributions $C_{mag}(T)$ of our samples (Fig. 11b and c) were determined by subtracting the lattice contributions $C_L(T)$ of nonmagnetic materials and electronic contributions $C_{el}(T)$ of $\text{Ba}_{8-x}\text{Eu}_x\text{Au}_y\text{Si}_{46-y}$ samples from total heat capacities $C_p(T)$. The magnetic entropies S_{mag} of 4.2 and 11.9 J K^{-1} per mole Eu for sample A and B, respectively, were calculated by integrating of $C_{mag}(T)$ up to corresponding T_C . These values reaches of $\approx 24\%$ and 69% of the theoretical value $R \ln(2S + 1)$, where R is the universal gas constant and $S = 7/2$ is the spin value for a free Eu^{2+} ion. High magnitude of S_{mag} clearly confirmed bulk origin of the magnetic phase transition, which can not be assigned to an influence of impurity states. The discrepancy between experimental and theoretical values of S_{mag} in $\text{Eu}_8\text{Ga}_{16}\text{Ge}_{30}$ was subscribed to the influence of tunneling of Eu^{2+} between the four equivalent sites in the large tetrakaidecahedral cage, which prevents the occurrence of a long-range FM ordering and favors the occurrence of a short-range FM ordering [24,37–39]. The tetrakaidecahedral cage in $\text{Ba}_{8-x}\text{Eu}_x\text{Au}_y\text{Si}_{46-y}$ is occupied only by Ba atoms. The discrepancy in our case is rather due to nonideal subtraction of digitized data of nonmagnetic reference samples from our $\text{Ba}_{8-x}\text{Eu}_x\text{Au}_y\text{Si}_{46-y}$ samples and their slight difference in compositions.

Finally, the lattice contribution of the heat capacity $C_L(T)$ was determined by subtracting of $C_{el}(T)$ and $C_{mag}(T)$ from the total heat capacity. $C_L(T)$ was fitted by the sum of one Debye Θ_D and two Einstein temperatures Θ_{E1}, Θ_{E2} (see Fig. 12) as presented in Ref. [40]. Two Einstein temperatures were required to describe the anisotropic guest vibrations in two pentagonal dodecahedra and six tetrakaidecahedra cages, respectively. Sum of Debye N_D and Einstein oscillators N_{Ei} were adjusted according to their number of atoms per formula unit. The fit parameters are summarized in Table 4. Data are in agreement with previous studies on $\text{Ba}_8\text{Au}_x\text{Si}_{46-x}$ [12]; the Debye temperature Θ_D and the lowest-lying Einstein temperature Θ_{E1} decreases with increasing the Au content,

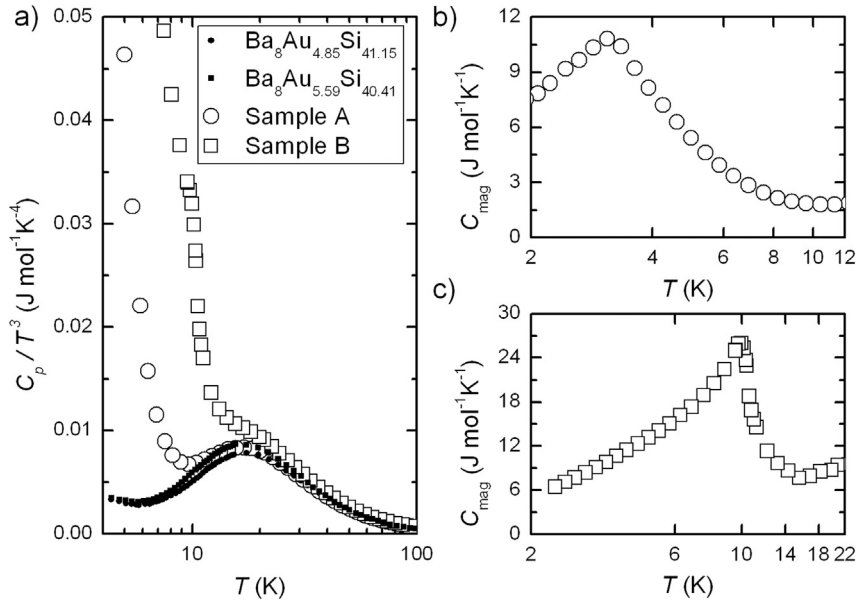


Fig. 11. (a) Temperature dependence of the heat capacities C_p/T^3 of $\text{Ba}_{8-x}\text{Eu}_x\text{Au}_y\text{Si}_{46-y}$ and their nonmagnetic compounds of $\text{Ba}_8\text{Au}_{4.85}\text{Si}_{39.72}$ and $\text{Ba}_8\text{Au}_{5.59}\text{Si}_{39.01}$ taken from Ref. [12]. (b) Temperature dependence of the magnetic contributions $C_{\text{mag}}(T)$ of sample A (b) and sample B (c).

Table 4
 $N(E_F)$ and γ parameters determined from the Hall coefficient, Θ_D , N_{E1} , N_{E2} , Θ_{E1} , and Θ_{E2} parameters determined from the heat capacities, and magnetic entropies S_{mag} per mole Eu calculated by integrating of $C_{\text{mag}}(T)$.

Code	$N(E_F)$ (states $(\text{eV f.u.})^{-1}$)	γ ($\text{mJ mol}^{-1}\text{K}^{-2}$)	Θ_D (K)	Θ_{E1} (K)	N_{E1} (const.)	Θ_{E2} (K)	N_{E2} (const.)	S_{mag} ($\text{J}(\text{K mol Eu})^{-1}$)
Sample A	6.0	14.2	360.9	82.3	0.7	82.8	6.1	4.2
Sample B	3.4	8.0	350.3	61.7	1.0	91.4	6.9	11.9

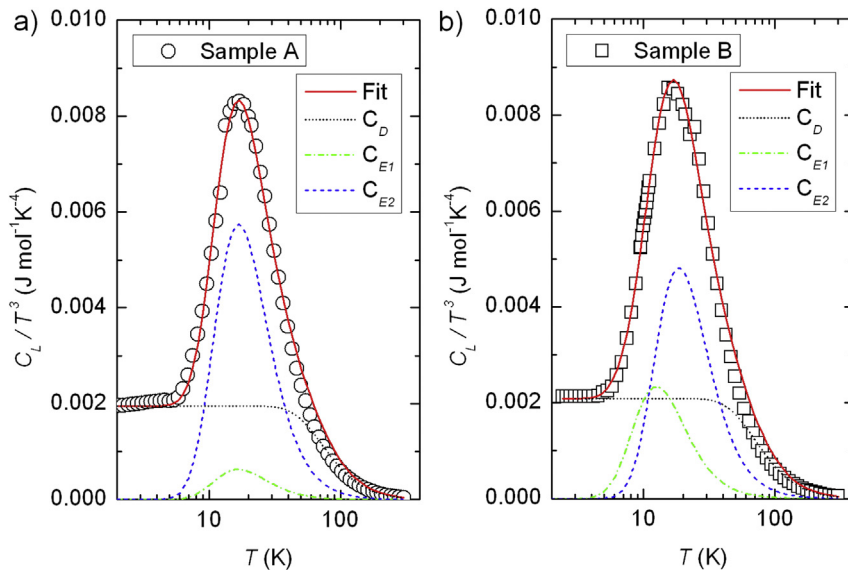


Fig. 12. Lattice contributions to the heat capacity C_L/T^3 as function of T for sample A (a) and sample B (b). The lines represent results from fitting using the model described in the text.

while Θ_{E2} increases.

Different scattering mechanisms have direct influence on the phonon relaxation time τ based on Matthiesen's rule $\tau^{-1} = \sum_i \tau_i^{-1}$. In order to determine which kind of scattering mechanism is

mainly responsible for a suppression of the maxima in κ_{ph} , Ikeda et al. proposed a modified Callaway model, in which the lowest-lying Einstein temperature Θ_{E1} and the average velocity of sound v , evaluated using the Debye temperature Θ_D and the lattice

parameter a as $v = (\Theta_D \cdot k_B)/[\hbar(6\pi^2 N/V)^{1/3}]$, where N is the number of atoms and V is the unit cell volume, are the main parameters for fitting the experimental data of κ_{ph} [41]. The model is valid well below Θ_{E1} ; in our case we used $T < (\Theta_{E1}/2)$. The average velocity of sound of 3332 m s⁻¹ and 3231 m s⁻¹ was evaluated for sample A and B, respectively, using Θ_D of 360.9 K and 350.3 K evaluated from the high-temperature fit of $C_L(T)$. The lowest-lying Einstein temperatures Θ_{E1} of 82.3 K and 61.7 K for sample A and B, respectively, were used for the fitting procedure. Ikeda et al. proposed in his model, that by increasing of the defect scattering rate, the maximum of phonon thermal conductivity $\kappa_{ph, max}$ is suppressed at $T = \text{const.}$, while the suppression of $\kappa_{ph, max}$ at $T \neq \text{const.}$ is either by increasing of the phonon-electron scattering rate or the boundary scattering rate [41]. The experimental $\kappa_{ph}(T)$ data of sample A were fitted using the modified Callaway model with Θ_{E1} and v values considering phonon-electron scattering, phonon-boundary scattering, phonon-defect scattering, and Umklapp scattering processes (Fig. 13). Possible reason for the glass-like behavior of sample B are strong phonon-electron interactions, observed also in Ba₈Ni_{6-x}Ge_{40+x} [34]. Therefore, the prefactors of all scattering rates except for the phonon-electron scattering rate for sample B were fixed to the prefactors of sample A. From the fit parameters (see Table 5), we conclude that: (i) linear-temperature dependence of κ_{ph} (T^1 power law in Fig. 13) indicates that Umklapp scattering is the dominant process at low temperatures. (ii) The phonon mean-free path $\bar{l} = v \cdot \tau$, where τ is the phonon relaxation time and v is the average velocity of sound, is, with $\approx 120 \mu\text{m}$ for both samples, indeed smaller than the size of the crystal. Therefore, phonon-boundary scattering is negligible in both samples. (iii) The prefactor of the phonon-electron scattering term is significantly enhanced for sample B, showing that this process is dominant and responsible for the glass-like κ_{ph} of *p*-type sample B.

Suekuni et al. published for type-I clathrates an universal dependency of the phonon thermal conductivity κ_{ph} at a constant temperature on the guest free space R_{free} (Fig. 14), defined as $R_{free} = R_{cage} - (r_{G-ion} + r_{H-cov}^{mean})$ [29,41], where R_{cage} is the distance between the 6d and 24k site, r_{G-ion} is the radius of the guest ion, and r_{H-cov} is the average value of the host atoms [41,42]. The covalent ionic radius of r_{Ba} (1.61 Å), r_{Eu} (1.35 Å), r_{Au} (1.37 Å), and r_{Si} (1.11 Å) were used from Refs. [23,29]. While the transition metal (TM) free type-I clathrates clearly show $\kappa_{ph}(R_{free})$ dependence indicated by the solid line, TM containing type-I clathrates revealed also $\kappa_{ph}(R_{free})$ trend, but different from TM free materials (see Fig. 14). Ba_{8-x}Eu_xAu_ySi_{46-y} samples lay within the error bar on the line of TM containing type-I clathrates. Reason why TM free- and TM containing type-I clathrates show different $\kappa_{ph}(R_{free})$ dependencies is due to fact that the bonding between TM of the framework and the guest atoms of Ba has additionally to the ionic character as well the covalent character compared to TM free type-I clathrates. This has been shown for example in Ba₈Au_{5.33}Ge₄₃ system [43].

The Ruderman-Kittel-Kasuya-Yoshida (RKKY) interactions are responsible for the ferromagnetic (FM) ordering of Ba_{8-x}Eu_xAu_ySi_{46-y} samples. It was shown for α - and β -Eu_{8-x}Ga₁₆

Table 5

Fit parameters of modified Callaway fits, where the scattering rates are phonon-electron scattering $\tau_{pe}^{-1} = A \cdot \omega^2$, phonon-boundary scattering $\tau_b^{-1} = B$, phonon-defect scattering $\tau_{pd}^{-1} = C \cdot \omega^4$, and Umklapp scattering $\tau_U^{-1} = D \cdot \omega^2 \cdot T \cdot \exp(\Theta_D - 3T)$. The values in the table are the constants A , B , C , and D .

Code	A (s)	B (s ⁻¹)	C (s ³)	D (sK ⁻¹)
Sample A	$1.09 \cdot 10^3$	$2.78 \cdot 10^7$	$5.26 \cdot 10^3$	$7.95 \cdot 10^5$
Sample B	$1.94 \cdot 10^8$	$2.78 \cdot 10^7$	$5.26 \cdot 10^3$	$7.95 \cdot 10^5$

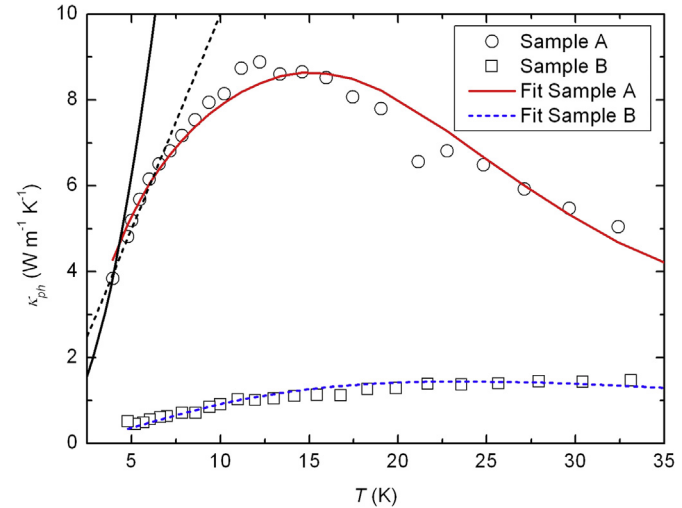


Fig. 13. Low-temperature κ_{ph} data of Ba_{8-x}Eu_xAu_ySi_{46-y} with the modified Callaway model fits. Black solid and short-dashed lines represents T^2 and T^1 power laws, respectively.

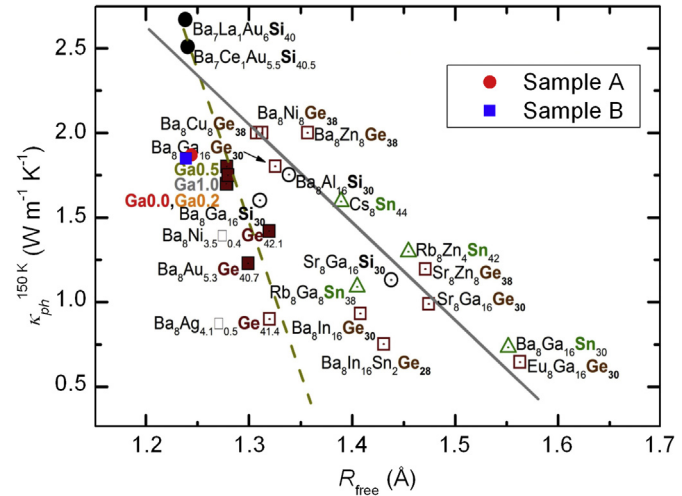


Fig. 14. Phonon thermal conductivity κ_{ph} at 150 K as function of the guest free space R_{free} of Ba_{8-x}Eu_xAu_ySi_{46-y} together with other type-I clathrates for comparison adapted from Ref. [41] and using data from Refs. [29,44–47]. Solid (TM free type-I clathrates) and dashed line (TM containing type-I clathrates) are guides for the eye.

Ge₃₀, that the shortest Eu-Eu distances lies within the first oscillation of the RKKY function [24], and thus can explain the FM behavior in both, α - and β -Eu_{8-x}Ga₁₆Ge₃₀. Additionally, calculating the $F(R)$ function within the RKKY formalism, where $J_{RKKY} \propto \sum_j [2k_F R_{ij} \cos(2k_F R_{ij}) - \sin(2k_F R_{ij})]/R_{ij}^4$, $k_F = (3\pi^2 n)^{1/3}$ and $F(R) = [2k_F R_{ij} \cos(2k_F R_{ij}) - \sin(2k_F R_{ij})]/R_{ij}^4$, the higher T_C for β -compared to α -Eu_{8-x}Ga₁₆Ge₃₀ was in agreement with higher absolute values of $F(R)$ [24]. Fig. 15 shows $F(R)$ functions for Ba_{8-x}Eu_xAu_ySi_{46-y} samples, calculated using the charge carrier concentrations at their T_C . Longer period of oscillation for sample B is due to smaller charge carrier concentration compared to sample A. Assuming the partial occupancy of Eu atoms at the 2a site, the nearest-neighbor (NN) Eu²⁺ (2a) - Eu²⁺ (2a) distance in both samples is $\approx 9.0 \text{ \AA}$. Using the sign convention of $F(R) < 0$, $S_i \cdot S_j > 0$ and $F(R) > 0$, $S_i \cdot S_j < 0$ for the ferromagnetic and antiferromagnetic (AFM)-type of order, respectively. $F(R)$ function at their

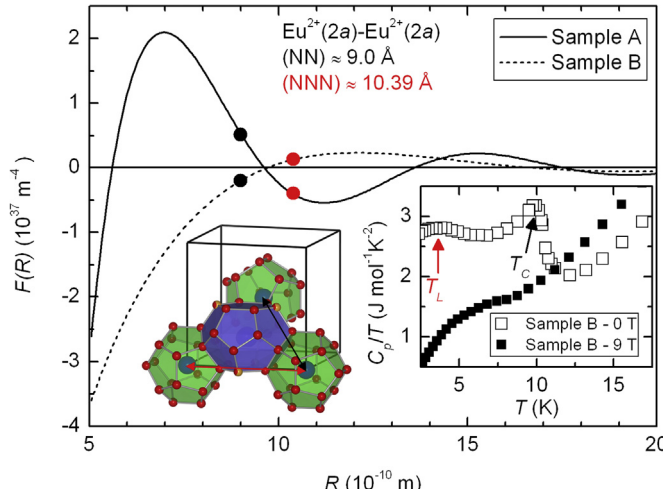


Fig. 15. $F(R) = [2k_F R_{ij} \cos(2k_F R_{ij}) - \sin(2k_F R_{ij})]/R_{ij}^4$ of $\text{Ba}_{8-x}\text{Eu}_x\text{Au}_y\text{Si}_{46-y}$ at their respective T_C as a function of the distance R from a given magnetic moment with spin S_i . Black and red solid circles represent the $F(R)$ functions for both samples at the nearest-neighbor (NN) and at the next-nearest-neighbor (NNN) Eu^{2+} (2a) - Eu^{2+} (2a) distances, respectively. The inset shows the temperature dependence of the heat capacity (C_p/T) of sample B measured in applied magnetic field of 0 T and 9 T. (For interpretation of the references to colour in this figure legend, the reader is referred to the web version of this article.)

Eu^{2+} (2a) - Eu^{2+} (2a) distances for both samples is, in absolute values, relatively small, compared to $\text{Eu}_8\text{Ga}_{16}\text{Ge}_{30}$ [24]. Furthermore, according to Fig. 15, sample A should exhibits an AFM-type of order, opposite to magnetic susceptibility measurements, which clearly demonstrate FM-type of order in both samples. Small and positive Weiss temperature of 6.0 K and 10.6 K for sample A and B, respectively, shows relatively small strength of FM-type of interactions, which can compete with an AFM-type of order. This could explain relatively small magnitude and different polarity of $F(R)$ function at their NN distances in our samples. The 2a lattice is exactly half-filled by Eu atoms in sample A. Therefore, the next-nearest-neighbor (NNN) Eu^{2+} (2a) - Eu^{2+} (2a) interaction at ≈ 10.39 Å are more probable compared to the nearest-neighbor (NN) at ≈ 9.0 Å, and thus the $F(R)$ function of sample A falls into negative FM regime (see Fig. 15). The scenario of preferable NNN interactions in sample A is supported by the fact that substituted Eu atoms, which create a local lattice distortion, avoid any clustering. Thus, probability of NNN interaction is enhanced. Large fraction of Eu atoms (84% occupancy) at the 2a site in sample B tends to prefer the NN interaction with an FM-type of order compared to a small fraction of an AFM-type of NNN interaction.

Phan et al. showed that $\text{Eu}_{8-x}\text{Sr}_x\text{Ga}_{16}\text{Ge}_{30}$ undergoes not only FM transition at $T_C \approx 35$ K, but also a secondary magnetic transition at $T_L \approx 10$ K [39], indicated as a result of the magnetic interaction between the Eu^{2+} at the 2a and the 6d site. The secondary magnetic transition in $\text{Eu}_8\text{Ga}_{16}\text{Ge}_{30}$ was observed e.g. as a broad shoulder in the magnetic heat capacity [24] and in the magnetic entropy change [39].

Heat capacity data plotted as C_p/T vs. T for sample B clearly exhibits an anomaly at $T_L \approx 3.7$ K (see inset of Fig. 15) compared to sample A with no observed anomaly (for clarity of Fig. 15 not shown). By applying external magnetic field of 9 T the secondary magnetic transition shifts towards higher temperatures (see inset of Fig. 15), which is a clear indication of no Kondo interactions presented in $\text{Ba}_{8-x}\text{Eu}_x\text{Au}_y\text{Si}_{46-y}$ samples, as it was shown in $\text{Ba}_6\text{Eu}_2\text{Al}_8\text{Si}_{36}$ system, where application of pressure up to 18 kbar enhances the magnetic ordering temperature [17]. The origin of secondary magnetic transition at 3.7 K in sample A might be due to

a small fraction of NN interaction, which gives an AFM-type of order.

5. Conclusions

Single-crystalline $\text{Ba}_{6.63 \pm 0.04}\text{Eu}_{1.0 \pm 0.04}\text{Au}_{4.77 \pm 0.10}\text{Si}_{41.60 \pm 0.11}$ and $\text{Ba}_{6.0 \pm 0.02}\text{Eu}_{1.68 \pm 0.04}\text{Au}_{5.32 \pm 0.06}\text{Si}_{41.0 \pm 0.04}$ samples were grown by a floating zone technique and investigated by measurements of the electrical resistivity, the Seebeck coefficient, the Hall coefficient, the heat capacity, the thermal conductivity, and the magnetic susceptibility. In agreement with the Zintl concept, n -type and p -type behavior for $\text{Ba}_{6.63}\text{Eu}_{1.0}\text{Au}_{4.77}\text{Si}_{41.6}$ and $\text{Ba}_{6.0}\text{Eu}_{1.68}\text{Au}_{5.32}\text{Si}_{41.0}$, respectively, was confirmed by Seebeck and Hall coefficient measurements. Both samples are metal-like and ferromagnetic with relatively low Curie temperatures. The RKKY interaction model was used in order to explain the FM-type of order in which the NNN and the NN interactions play a major role in sample A and B, respectively. The thermal conductivity of $\text{Ba}_{6.63 \pm 0.04}\text{Eu}_{1.0 \pm 0.04}\text{Au}_{4.77 \pm 0.10}\text{Si}_{41.60 \pm 0.11}$ shows a large maximum at low temperatures, which is drastically suppressed for $\text{Ba}_{6.0 \pm 0.02}\text{Eu}_{1.68 \pm 0.04}\text{Au}_{5.32 \pm 0.06}\text{Si}_{41.0 \pm 0.04}$. From the modified Callaway model, proposed by Ikeda et al. [41], we concluded that Umklapp scattering process is dominant at low temperatures for both samples and enhanced phonon-electron scattering in $\text{Ba}_{6.0 \pm 0.02}\text{Eu}_{1.68 \pm 0.04}\text{Au}_{5.32 \pm 0.06}\text{Si}_{41.0 \pm 0.04}$ is responsible for the large suppression of the thermal conductivity.

Acknowledgements

We acknowledge support from the Austrian Science Fund (FWF project TRP 176-N22), the German Research Foundation (DFG project SPP 1c386-nanOcla), and the European Integrated Center for the Development of New Metallic Alloys and Compounds (C-MAC). We thank M. Ikeda for useful discussions. We thank R. Svagera and M. Waas for the SEM/EDX analysis.

References

- [1] A. Bentien, E. Nishibori, S. Paschen, B. Iversen, Crystal structures, atomic vibration, and disorder of the type-I thermoelectric clathrates $\text{Ba}_8\text{Ga}_{16}\text{Si}_{30}$, $\text{Ba}_8\text{Ga}_{16}\text{Ge}_{30}$, $\text{Ba}_8\text{In}_{16}\text{Ge}_{30}$, and $\text{Sr}_8\text{Ga}_{16}\text{Ge}_{30}$, Phys. Rev. B 71 (2005) 144107.
- [2] L. Nguyen, U. Aydemir, M. Baitinger, E. Bauer, H. Borrmann, U. Burkhardt, J. Custers, A. Haghvirad, R. Höfler, K. Luther, F. Ritter, W. Assmus, Y. Grin, S. Paschen, Atomic ordering and thermoelectric properties of the n-type clathrate $\text{Ba}_8\text{Ni}_{3.5}\text{Ge}_{42.1}\square_{0.4}$, Dalton Trans. 39 (2010) 1071–1077.
- [3] M. Christensen, A. Abrahamsen, N. Christensen, F. Juranyi, N. Andersen, K. Lefmann, C. Andreasson, B. Bahl, Iversen, Avoided crossing of rattler modes in thermoelectric materials, Nat. Mater. 7 (2008) 811–815.
- [4] H. Euchner, S. Pailhès, L. Nguyen, W. Assmus, F. Ritter, A. Haghvirad, Y. Grin, S. Paschen, M. De Boissieu, Phononic filter effect of rattling phonons in the thermoelectric clathrate $\text{Ba}_8\text{Ge}_{40+x}\text{Ni}_{6-x}$, Phys. Rev. B 86 (2012) 224303.
- [5] H.J. Goldsmid, Thermoelectrics Handbook: Macro to Nano, CRC, Boca Raton, FL, 1995.
- [6] A. Saramat, G. Svensson, A. Palmqvist, C. Stiewe, E. Mueller, D. Platzek, S. Williams, D. Rowe, J. Bryan, G. Stucky, Large thermoelectric figure of merit at high temperature in Czochralski-grown clathrate $\text{Ba}_8\text{Ga}_{16}\text{Ge}_{30}$, J. Appl. Phys. 99 (2006) 023708.
- [7] J. Martin, H. Wang, G. Nolas, Optimization of the thermoelectric properties of $\text{Ba}_8\text{Ga}_{16}\text{Ge}_{30}$, Appl. Phys. Lett. 92 (2008) 222110.
- [8] V. Kuznetsov, L. Kuznetsova, A. Kalazin, D. Rowe, Preparation and thermoelectric properties of $\text{A}_8\text{II}\text{B}_{16}\text{III}\text{B}_{30}$ IV clathrate compounds, J. Appl. Phys. 87 (2000) 7871–7875.
- [9] X. Yan, M. Chen, S. Laumann, E. Bauer, P. Rogl, R. Podloucky, S. Paschen, Thermoelectric properties of Ba-Cu-Si clathrates, Phys. Rev. B 85 (2012) 165127.
- [10] X. Yan, E. Bauer, P. Rogl, S. Paschen, Structural and thermoelectric properties of $\text{Ba}_8\text{Cu}_5\text{Si}_x\text{Ge}_{41-x}$ clathrates, Phys. Rev. B 87 (2013) 115206.
- [11] C. Candolfi, U. Aydemir, M. Baitinger, N. Oeschler, F. Steglich, Y. Grin, High temperature thermoelectric properties of the type-I clathrate $\text{Ba}_8\text{Au}_x\text{Si}_{46-x}$, J. Appl. Phys. 111 (2012) 043706.
- [12] U. Aydemir, C. Candolfi, A. Ormeci, Y. Oztan, M. Baitinger, N. Oeschler, F. Steglich, Y. Grin, Low-temperature thermoelectric, galvanomagnetic, and thermodynamic properties of the type-I clathrate $\text{Ba}_8\text{Au}_x\text{Si}_{46-x}$, Phys. Rev. B 84 (2011) 195137.

- [13] S. Yamanaka, E. Enishi, H. Fukuoka, M. Yasukawa, High-pressure synthesis of a new silicon clathrate superconductor, $\text{Ba}_8\text{Si}_{46}$, Inorg. Chem. 39 (2000) 56–58.
- [14] S. Yamanaka, Silicon clathrates and carbon analogs: high pressure synthesis, structure, and superconductivity, Dalton Trans. 39 (2010) 1901–1915.
- [15] J. Cohn, G. Nolas, V. Fessatidis, T. Metcalf, G. Slack, Glasslike heat conduction in high-mobility crystalline semiconductors, Phys. Rev. Lett. 82 (1999) 779–782.
- [16] G. Woods, J. Martin, M. Beekman, R. Hermann, F. Grandjean, V. Keppens, O. Leupold, G. Long, G. Nolas, Magnetic and electronic properties of $\text{Eu}_8\text{Sr}_4\text{Ga}_{16}\text{Ge}_{30}$, Phys. Rev. B 73 (2006).
- [17] Y. Mudryk, P. Rogl, C. Paul, S. Berger, E. Bauer, G. Hilscher, C. Godart, H. Noël, Thermoelectricity of clathrate i si and ge phases, J. Electron. Mater. 14 (2002) 7991–8004.
- [18] Y. Zhang, P. Lee, G. Nolas, A. Wilkinson, Gallium distribution in the clathrates $\text{Sr}_8\text{Ga}_{16}\text{Ge}_{30}$ and $\text{Sr}_4\text{Eu}_4\text{Ga}_{16}\text{Ge}_{30}$ by resonant diffraction, Appl. Phys. Lett. 80 (2002) 2931–2933.
- [19] A. Prokofiev, R. Svagera, M. Waas, M. Weil, J. Bernardi, S. Paschen, Mechanism of rare earth incorporation and crystal growth of rare earth containing Type-I clathrates, Cryst. Growth Des. 16 (2016) 25–33.
- [20] J. Rodriguez-Carvajal, Recent advances in magnetic structure determination by neutron powder diffraction, Phys. B 192 (1993) 55–69.
- [21] A. Prokofiev, A. Sidorenko, K. Hradil, M. Ikeda, R. Svagera, M. Waas, H. Winkler, K. Neumaier, S. Paschen, Thermopower enhancement by encapsulating cerium in clathrate cages, Nat. Mater. 12 (2013) 1096–1101.
- [22] E. Parthé, L. Gelato, B. Chabot, M. Penzo, K. Cenzual, R. Gladyshevskii, TZPIX Standardized Data and Crystal Chemical Characterization of Inorganic Structure Types, Springer, New York, 1994.
- [23] R. Shannon, Revised effective ionic radii and systematic studies of interatomic distances in halides and chalcogenides, Acta Crystallogr. Sect. A 32 (1976) 751–767.
- [24] S. Paschen, W. Carrillo-Cabrera, A. Bentien, V. Tran, M. Baenitz, Y. Grin, F. Steglich, Structural, transport, magnetic, and thermal properties of $\text{Eu}_8\text{Ga}_{16}\text{Ge}_{30}$, Phys. Rev. B 64 (2001) 214404.
- [25] E. Nagaev, E. Sokolova, Anomalous hall effect in ferromagnetic semiconductors, Sov. Phys.-Sol. State 19 (1977) 425–429.
- [26] S. Paschen, V. Tran, M. Baenitz, W. Carrillo-Cabrera, Y. Grin, F. Steglich, Clathrate $\text{Ba}_8\text{Ge}_{25}$: thermodynamic, magnetic, and transport properties, Phys. Rev. B 65 (2002) 1344351–1344359.
- [27] S. Christensen, M. Avila, K. Suekuni, R. Piltz, T. Takabatake, M. Christensen, Combined X-ray and neutron diffraction study of vacancies and disorder in the dimorphic clathrate $\text{Ba}_8\text{Ga}_{16}\text{Sn}_{30}$ of type I and VIII, Dalton Trans. 42 (2013) 14766–14775.
- [28] S. Laumann, M. Ikeda, H. Sassik, A. Prokofiev, S. Paschen, Meltspun $\text{Ba}_8\text{G}-\text{a}_{16-x}\text{Ge}_{30+x}$ clathrates, J. Mater. Res. 26 (2011) 1861.
- [29] K. Suekuni, S. Yamamoto, M. Avila, T. Takabatake, Universal relation between guest free space and lattice thermal conductivity reduction by anharmonic rattling in type-I clathrates, J. Phys. Soc. Jpn. 77 (2008) 61–66.
- [30] M. Ikeda, X. Yan, L. Prochaska, G. Lientschnig, R. Svagera, M. Waas, P. Tomeš, A. Prokofiev, E. Bauer, S. Paschen, Thermal conductivity of transition metal containing type-I clathrates, in: Symposium S/W/CC Advanced Materials for Photovoltaic, Fuel Cell and Electrolyzer, and Thermoelectric Energy Conversion, 1735, MRS Online Proceedings Library Archive, 2015, <http://dx.doi.org/10.1557/pl.2015.269>.
- [31] Z. Ye, J. Cho, M. Tessema, J. Salvador, R. Waldo, J. Yang, H. Wang, W. Cai, M. Kirkham, J. Yang, W. Zhang, Thermoelectric properties of Au-containing type-I clathrates $\text{Ba}_8\text{Au}_x\text{Ga}_{16-3x}\text{Ge}_{30+2x}$, J. Alloys Compd. 587 (2014) 747–754.
- [32] M. Bentien, A. Christensen, J. Bryan, A. Sanchez, S. Paschen, F. Steglich, G. Stucky, B. Iversen, Thermal conductivity of thermoelectric clathrates, Phys. Rev. B 69 (2004) 451071–451075.
- [33] M. Christensen, N. Lock, J. Overgaard, B. Iversen, Crystal structures of thermoelectric n- and p-type $\text{Ba}_8\text{Ga}_{16}\text{Ge}_{30}$ studied by single crystal, multi-temperature, neutron diffraction, conventional X-ray diffraction and resonant synchrotron X-ray diffraction, J. Am. Chem. Soc. 128 (2006) 15657–15665.
- [34] A. Bentien, S. Johnsen, B. Iversen, Strong phonon charge carrier coupling in thermoelectric clathrates, Phys. Rev. B 73 (2006) 094301.
- [35] L. Liu, B. Song, B. Sun, H. Ma, X. Ma, Y. Li, High-pressure synthesis and properties of the Eu-substituted $\text{Ba}_8-x\text{Eu}_x\text{Si}_{46}$ clathrates, Phys. B 485 (2016) 84–88.
- [36] C. Kittel, Introduction to Solid State Physics, fourth ed., John Wiley and Sons, Inc., New York, 1966.
- [37] T. Onimaru, S. Yamamoto, M.A. Avila, K. Suekuni, T. Takabatake, Multiple ferromagnetic structures in an off-center rattling system $\text{Eu}_8\text{Ga}_{16}\text{Ge}_{30}$, J. Phys. Conf. Ser. 200 (2010) 022044.
- [38] B. Sales, B. Chakoumakos, R. Jin, J. Thompson, D. Mandrus, Structural, magnetic, thermal, and transport properties of $\text{X}_8\text{Ga}_{16}\text{Ge}_{30}$ ($\text{X} = \text{Eu}, \text{Sr}, \text{Ba}$) single crystals, Phys. Rev. B 63 (2001) 245113.
- [39] M.-H. Phan, V. Franco, A. Chaturvedi, S. Stefanoski, G. Nolas, H. Srikanth, Origin of the magnetic anomaly and tunneling effect of europium on the ferromagnetic ordering in $\text{Eu}_{8-x}\text{Sr}_x\text{Ga}_{16}\text{Ge}_{30}$ ($x=0.4$) type-I clathrates, Phys. Rev. B 84 (2011) 054436.
- [40] P. Tomeš, X. Yan, R. Kastner, R. Svagera, M. Waas, J. Eilertsen, A. Weidenkaff, S. Paschen, Thermoelectric properties of meltspun $\text{Ba}_8\text{Cu}_5(\text{Si}, \text{Ge}, \text{Sn})_{41}$ clathrates, J. Alloys Compd. 654 (2016) 300–307.
- [41] M. Ikeda, Mechanism of the Thermal Conductivity of Type-I Clathrates, Ph.D. thesis, TU Wien, 2015.
- [42] G.S. Nolas, The Physics and Chemistry of Inorganic Clathrates, Springer Netherlands, 2014.
- [43] H. Zhang, H. Borrmann, N. Oeschler, C. Candolfi, W. Schnelle, M. Schmidt, U. Burkhardt, M. Baitinger, J.-T. Zhao, Y. Grin, Atomic interactions in the p-type clathrate I $\text{Ba}_8\text{Au}_{5.3}\text{Ge}_{40.7}$, Inorg. Chem. 50 (2011) 1250–1257.
- [44] M.G. Holland, Analysis of lattice thermal conductivity, Phys. Rev. 132 (1963) 2461.
- [45] Y. Saiga, K. Suekuni, B. Du, T. Takabatake, Thermoelectric properties and structural instability of type-I clathrate $\text{Ba}_8\text{Ga}_{16}\text{Sn}_{30}$ at high temperatures, Solid State Commun. 152 (2012) 1902.
- [46] I. Zeiringer, M. Chen, I. Bednar, E. Rojanian, E. Bauer, R. Podloucky, A. Grytsiv, P. Rogl, H. Effenberger, Phase equilibria, crystal chemistry, electronic structure and physical properties of Ag-Ba-Ge clathrates, Acta Mater. 59 (2011) 2368–2384.
- [47] G.S. Nolas, T.J.R. Weakley, J.L. Cohn, Structural, chemical, and transport properties of a new clathrate compound: $\text{Cs}_8\text{Zn}_4\text{Sn}_{42}$, Chem. Mater. 11 (1999) 2470.